

Geophysical Research Letters

RESEARCH LETTER

10.1029/2019GL081916

Key Points:

- Geodetic velocity field shows spatially variable strain within south-central Tibet
- Strain rates are similar outside and inside the mapped fault zones
- Conjugate strike-slip faults in south-central Tibet have low slip rates (≤ 4 mm/year)

Supporting Information:

- Supporting Information S1
- Data Set S1

Correspondence to:

H. Wang,
ehwang@163.com

Citation:

Wang, H., Wright, T. J., Liu-Zeng, J., & Peng, L. (2019). Strain rate distribution in south-central Tibet from two decades of InSAR and GPS. *Geophysical Research Letters*, 46, 5170–5179. <https://doi.org/10.1029/2019GL081916>

Received 4 JAN 2019

Accepted 25 APR 2019

Accepted article online 1 MAY 2019

Published online 21 MAY 2019

Strain Rate Distribution in South-Central Tibet From Two Decades of InSAR and GPS

Hua Wang¹ , Tim J. Wright² , Jing Liu-Zeng^{3,4} , and Lincai Peng¹

¹Department of Surveying Engineering, Guangdong University of Technology, Guangzhou, China, ²COMET, School of Earth and Environment, University of Leeds, Leeds, UK, ³State Key Laboratory of Earthquake Dynamics, Institute of Geology, China Earthquake Administration, Beijing, China, ⁴Institute of Surface-Earth System Science, Tianjin University, Tianjin, China

Abstract The degree to which deformation and seismicity is focused on major mapped structures remains a key unknown in assessing seismic hazards and testing continental deformation models. Here we combine 208 Global Positioning System (GPS) velocities with 12-track Interferometric Synthetic Aperture Radar (InSAR) rate maps to form high-resolution velocity and strain rate fields for south-central Tibet. Our results show that deformation is not evenly distributed across the region. We find a few zones with high strain rates, most notably the Yutian-Zhongba strain rate zone. However, the average of the strain rates is similar within and outside the mapped fault zones. In addition, the slip rates are low on all the conjugate strike-slip faults widespread in central Tibet. The observations are difficult to reconcile with time-invariant block models or with continuum models that lack mechanisms for strain localization. Our results support arguments that the most robust estimates of seismic hazard should integrate seismicity catalogues, active fault maps, and geodetic strain rate models.

1. Introduction

The ongoing collision between India and Asia has created the Tibetan Plateau, the largest deforming area on the planet with widespread earthquakes and active faults (Molnar & Tapponnier, 1975). The plateau is an ideal natural laboratory for studying continental tectonics. Despite decades of study, the degree to which deformation is best modeled as a continuum (England & Houseman, 1986; England & Molnar, 1997; 2005) or as large discrete blocks (Avouac & Tapponnier, 1993; Chen et al., 2004; Liu & Bird, 2008; Loveless & Meade, 2011; Meade, 2007; Tapponnier et al., 1982; Thatcher, 2007) remains unclear. This is important for seismic hazard assessment as it governs the degree to which seismic hazard in continental interiors is focused around major tectonic structures (England & Jackson, 2011; Jackson, 2001). High-resolution geodetic velocity field can be used to test this question (England & Molnar, 2005; Thatcher, 2007) and to improve seismicity forecasts (Bird et al., 2010; Field et al., 2014; Zheng et al., 2018).

The Global Positioning System (GPS) has been widely used to determine the velocity field of Tibet (Zheng et al., 2017, and references therein). The number of GPS sites has increased in the last two decades, supported mainly by the CMONOC-I/II projects (Zheng et al., 2017). Nevertheless, the current data sets are still sparse and large gaps between stations exist in areas such as south-central Tibet, due to the challenges of access in remote and sparsely populated regions. Interferometric Synthetic Aperture Radar (InSAR) has been shown to be able to measure large-scale deformation with similar accuracy to GPS (Elliott et al., 2016). Although InSAR only measures the scalar velocity in the satellite's line of sight (LOS), the method has high resolution (tens of meters) and does not require measurements in the field. InSAR can therefore complement GPS measurements. Wang and Wright (2012) developed a method to determine high-resolution velocity fields by combining GPS and InSAR data, which has since been applied to other large regions including Afar (Pagli et al., 2014) and eastern Turkey (Walters et al., 2014).

Our study area comprises south-central Tibet, from 80° to 92° E and between the Jinsha Suture (JS) in the north and the Indus-Yalu Suture (IYS) in the south (Figure 1a). The major structures include a set of conjugate strike-slip faults in the central part of the region and a series of north-south rifts that cross the southern part of the region. The conjugate faults strike at a small angle to and on two sides of the east-trending Bangong-Nujiang Suture (BNS) at $\sim 32^{\circ}$ N. They are composed of northeast-striking sinistral faults in the

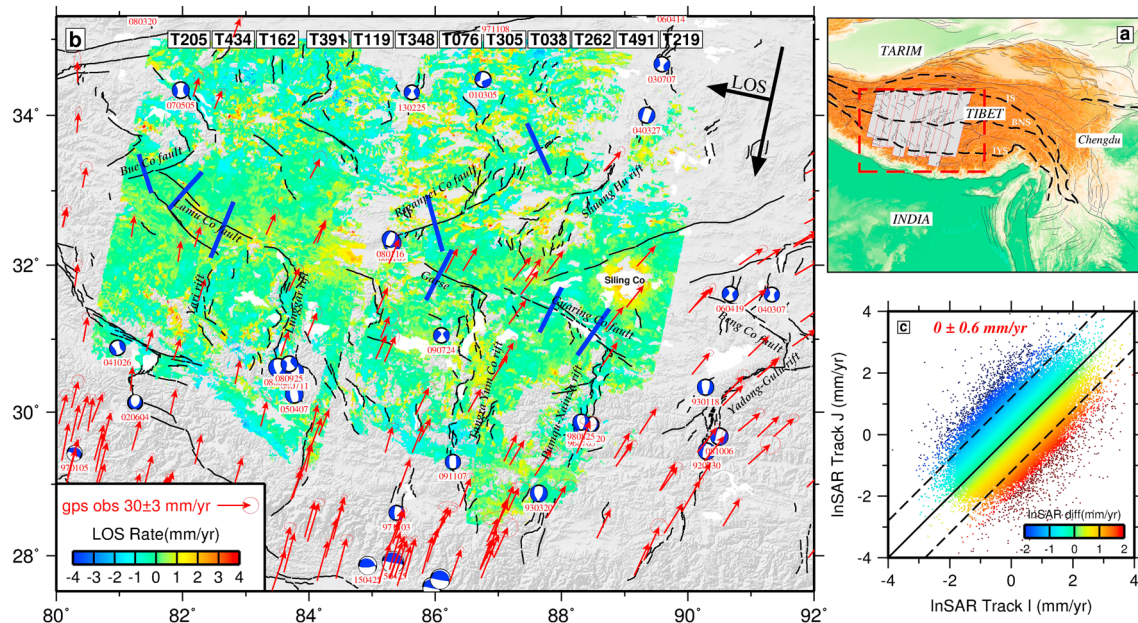


Figure 1. (a) Topographic and tectonic map of the Tibetan Plateau. The red box indicates the area of Figure 1b. The gray rectangles delimit the extents of the ERS-1/2 and Envisat radar imagery on 12 descending tracks. (b) Line-of-sight InSAR rate maps and horizontal Global Positioning System velocities in south-central Tibet. “Beach-balls” marked by red numbers beneath represent focal mechanisms and dates of occurrence (YYMMDD) of the $M_w \geq 5.5$ earthquakes since 1992. Black lines are major faults from Taylor and Yin (2009). The long and short black arrows indicate satellite flight and look directions, respectively. Blue lines show the locations of cross-fault velocity profiles. (c) Scatterplot shows the differences of InSAR rate maps between neighboring tracks. Dashed lines show 2σ bounds of the differences. InSAR = interferometric synthetic aperture radar; LOS = line of sight.

north and northwest-striking dextral faults in the south (Armijo et al., 1989; Taylor et al., 2003). Many of the conjugate faults intersect with the widespread NS-trending rifts on the south side of the BNS (Armijo et al., 1986). Collectively, these faults accommodate north-south convergence and east-west extension within the collision zone (Armijo et al., 1986, 1989; Molnar & Tapponnier, 1978; Styron et al., 2011; Taylor & Yin, 2009). Many strike-slip and normal earthquakes have occurred in the region (Molnar & Lyon-Caen, 1989), but recent normal earthquakes have not all been associated with the major grabens (e.g., Elliott et al., 2010; Wang et al., 2014). Therefore, an open question is the degree to which strain is focused on the major mapped structures and the degree to which deformation occurs in a more distributed fashion outside them.

In this study, we estimate velocity and strain rate fields for south-central Tibet by combining the full archive of radar acquisitions from the European Space Agency’s ERS-1/2 and Envisat satellites with the latest GPS velocities (Zheng et al., 2017). InSAR works well in south-central Tibet where there is a large archive of long-term radar observations, relatively low atmospheric delay variations, and high coherence due to the lack of vegetation (Garthwaite et al., 2013; Ryder et al., 2014). We use the resultant velocity and strain rate fields to derive fault slip rates and to test the degree to which strain is focused on the major faults. We discuss the implications for models of continental deformation and for seismic hazard in continental interiors.

2. InSAR Interseismic Rate Maps

Between 1992 and 2010, European Space Agency’s ERS-1/2 and Envisat satellites acquired hundreds of radar images over Tibet. Using the Jet Propulsion Laboratory/Caltech ROI_PAC software (Rosen et al., 2004), we processed 93 ERS-1/2 (1992–2000) and 330 Envisat (2003–2010) acquisitions on 12 descending tracks, each covering an area ~ 100 km wide and ~ 700 km long (Figure 1). Relatively few images were acquired on ascending tracks in this region, which prevented us from making useful ascending rate maps. We formed interferometric pairs with short temporal and perpendicular baselines to maximize coherence; Figure S1 in the supporting information shows all the epochs and the baselines of the processed pairs. We removed the topographic phase contribution using precise orbits and the 3-arc sec (~ 90 m) Shuttle Radar Topography Mission Digital Elevation Model (Farr et al., 2007). We smoothed the interferograms using 4-range by 20-azimuth multilook processing and by applying an adaptive power spectrum filter (Goldstein & Werner, 1998). We carefully unwrapped the phase in each interferogram with a conservative branch-cut method

(Goldstein et al., 1988). We connected isolated patches of unwrapped phase by manually setting up bridges. We checked and corrected phase unwrapping errors manually using a phase closure technique (Biggs et al., 2007; Wang et al., 2012). We finally selected 626 geocoded interferograms in total for rate map estimation, discarding interferograms where fewer pixels had been successfully unwrapped.

We estimated rate maps (average LOS velocities) at \sim 450-m spacing for each track individually using the multi-interferogram method (Biggs et al., 2007) implemented as Poly-Interferogram Rate And Time-series Estimator (*PITRATE*) software (Wang et al., 2012). Based on the network approach (Biggs et al., 2007; Elliott et al., 2008), we corrected long-wavelength orbital and atmospheric errors with a quadratic function of coordinates and topographically correlated atmospheric delay errors with a linear function of topography. On a pixel-by-pixel basis, we then estimated LOS velocity and its uncertainty using an iterative weighted least squares approach (Wang et al., 2009), where the full spatiotemporal weight matrix was determined using an exponentially decaying function (Biggs et al., 2007; Parsons et al., 2006). During the radar observation period, $33 M_w \geq 5.5$ earthquakes occurred in the study area (Figure 1b). To exclude effects of these earthquakes, we manually masked the areas in the interferograms with coseismic and/or potential rapid postseismic deformation transients. We were conservative to set larger areas and longer time spans than that the earthquakes might affect by comparing the resultant rate maps with different masks. Long-lived postseismic deformation transients (e.g., Ingleby & Wright, 2017) may be present, but there have not been any large earthquakes ($M > 7$) in this region in the last 85 years. Therefore, our resultant rate maps in Figure 1b represent average deformation measured over a two-decade time period. Note that any long-wavelength deformation was also removed from the rate maps while correcting orbital and atmospheric delay errors. Figure 1c shows scatterplot of InSAR LOS velocities between neighboring tracks. The mean and the standard deviation of velocity differences are 0 and 0.6 mm/year, respectively, and the correlation coefficient is 0.7, indicating consistency between the rate maps. Our results cover the largest velocity field determined by InSAR to date, spanning a region \sim 1,000 km by \sim 700 km with nearly complete coverage. Figure S2 shows the formal 1σ errors of InSAR rate maps.

One prominent feature is a bowl-shape subsidence signal with radius of \sim 40 km and amplitude of 3 mm/year surrounding the Siling Co (Figure 1b). Figure S3 shows the signal, with consistent results observed in two neighboring tracks; the maximum rate difference is less than 1 mm/year. Doin et al. (2015) discussed this signal and suggested the cause was hydrological loading associated with recent water level changes in the lake. Our results show similar patterns to those in Doin et al. (2015), but our rates are slightly smaller, probably because we did not use ERS interferograms from 2000 to 2003, when Doin et al. (2015) found the most rapid lake level rise.

3. Velocity and Strain Rate Fields

Using the velocity field inversion method described in Wang and Wright (2012), we made a continuous horizontal velocity field across south-central Tibet by combining 12 tracks of InSAR rate maps and 208 GPS velocities from Zheng et al. (2017). Prior to the inversion, we multilooked the InSAR rate maps to reduce the data to \sim 4.5-km spacing (Figure S4). We divided the region into a triangular mesh with 779 vertices at 30- to 50-km spacing (Figure S5a) and assumed the velocity varies linearly with latitude and longitude within each triangle. The observed InSAR and GPS velocities are then related to that of the enclosing three vertices via a spherical shape function (England & Molnar, 2005). For the flattened InSAR rate maps, we introduced a quadratic function of coordinates and a linear function of topography to retrieve long-wavelength deformation via joint inversion of GPS and InSAR data following equation 1 in Wang and Wright (2012). To avoid oscillation of solutions and effects of short-wavelength nontectonic signals, we constrained the modeled velocities using Laplacian smoothing approximated by a scale-dependent umbrella operator (Desbrun et al., 1999). The smoothing factor was selected using a trade-off curve between solution roughness and weighted misfit (Figure S6). We solved the system of equations using a biconjugate gradients method to yield velocities of the vertices, as well as long-wavelength correction terms for the InSAR data.

Liang et al. (2013) showed that the relative vertical velocities from GPS are less than 2 mm/year in the area covered by our InSAR data, similar to the values found by combining GPS and InSAR in western Tibet (Wang & Wright, 2012). We therefore chose to assume vertical velocities are negligible and solve for only the horizontal components of the velocity field. Wang and Wright (2012) found that the east components from a full 3-D velocity field inversion were nearly identical to those found when inverting for only horizontal veloci-

ties. We also note that vertical deformation around Siling Co does not contaminate the horizontal velocity field significantly, with the vertical deformation signals appearing in the residual rate maps (Figure S7).

Systematic bias of uncertainties is a long-standing issue in geodetic joint inversions. We formed an initial covariance matrix of GPS data using their formal uncertainties and that of InSAR data using an exponentially decaying spatial covariance function (Parsons et al., 2006), as in Wang and Wright (2012). Then we iteratively estimated a scalar factor to update the covariance of GPS and InSAR data using a variance component estimation approach (Grafarend, 1985). The final estimates of variance factors are 1.7 and 4.4 for GPS and InSAR, respectively, implying both formal errors are underestimated.

With the velocities of the vertices, we can make a continuous horizontal velocity field using the shape functions (England & Molnar, 2005) and a strain rate field using spherical approximation equations (Savage et al., 2001; Figure 2). Figure S8 shows the synthetic InSAR LOS velocities including the long-wavelength components. The final root-mean-square misfit between the observations and the velocity field model is 1.3 mm/year for the GPS horizontal velocities and 0.7 mm/year for the InSAR LOS rate maps. Figure S9 shows velocity residuals between LOS InSAR and GPS with long-wavelength deformation removed. The residuals are small, and there is no clear systematic spatial distribution. This supports our assumption of negligible vertical deformation in velocity field inversion. Figure S10 shows 1σ errors of the strain rate fields by propagation of InSAR and GPS errors. The average of relative 1σ error is $\sim 23\%$. Large uncertainties lie in the north, where there are no GPS data at all. We also note that the result is somewhat dependent on the mesh size. A larger mesh size results in a smoother result (Figure S5). We selected a mesh size of 30 km where there is InSAR data and 50 km elsewhere. This spacing gives us a regional velocity field that is sufficiently dense to identify strain associated with individual faults.

As found in Wang and Wright (2012), much more detailed deformation signals are resolved in the velocity field fitted with InSAR and GPS data (Figure 2) than that from GPS alone (Figure S11), particularly for the east-west components, where InSAR makes the biggest contribution. Meanwhile, the uncertainties of the estimated east and north components are also decreased by up to 43% and 14%, respectively, particularly in areas far away from the GPS sites (Figures S12). As expected, the highest strain rates lie along the Himalayan arc and are associated with rapid convergence of India-Eurasia collision (e.g., Zheng et al., 2017). Our results also reveal a few zones with elevated strain rates away from the Himalaya, most notably a NNW-SSE elongated zone that spans the entire study area from Yutian to Zhongba (named as YZSZ in following text, Figure 2).

4. Analysis of Velocity Field

4.1. Slip Rates of the Conjugate Strike-Slip Faults

The network of conjugate strike-slip faults is the dominant structures in central Tibet (Armijo et al., 1989; Taylor et al., 2003). However, the slip rates of these faults are poorly known. Early geological investigations suggested rapid slip of up to 1–2 cm/year in the fault systems (Armijo et al., 1989), while recent InSAR and geological studies suggested much lower slip rates (Garthwaite et al., 2013; Shi et al., 2014). To the best of our knowledge, Taylor and Peltzer (2006) is the only study who used geodesy to constrain interseismic slip rates and locking depths of the conjugate strike-slip faults in our study area. Nevertheless, their results relied on very limited number of interferograms (mostly one interferometric pair), thus are susceptible to atmospheric delay errors.

We estimated the slip rates across six major strike-slip faults using ± 30 -km-long profiles (Figures 1b and 3) from the InSAR LOS rate maps at ~ 450 -m spacing, including the long-wavelength deformation from GPS/InSAR joint inversion. We used a simple elastic dislocation model (Savage & Burford, 1973), assuming a fixed locking depth of 10 km consistent with coseismic studies in the region (Wright et al., 2013). The right-lateral slip rates are 1 ± 0.3 and 4 ± 0.4 mm/year on the west and east segment of the Gyaring Co fault, respectively (Figures 3a and 3b). The results are generally consistent with recent geological investigations, which found rate of 2.2–4.5 mm/year along the central Gyaring Co fault since mid-Holocene (Shi et al., 2014) but significantly lower than the early InSAR estimate of 10–18 mm/year from Taylor and Peltzer (2006). The large discrepancy is most likely due to atmospheric delay errors in Taylor and Peltzer (2006), which was only based on one interferogram. Correspondingly, the associated locking depth of 23–27 km in Taylor and Peltzer (2006) is also inconsistent with coseismic studies in Tibet (Wright et al., 2013). We found no apparent strain accumulation on the Garse fault lying at further west of the Gyaring Co fault (Figure 3c).

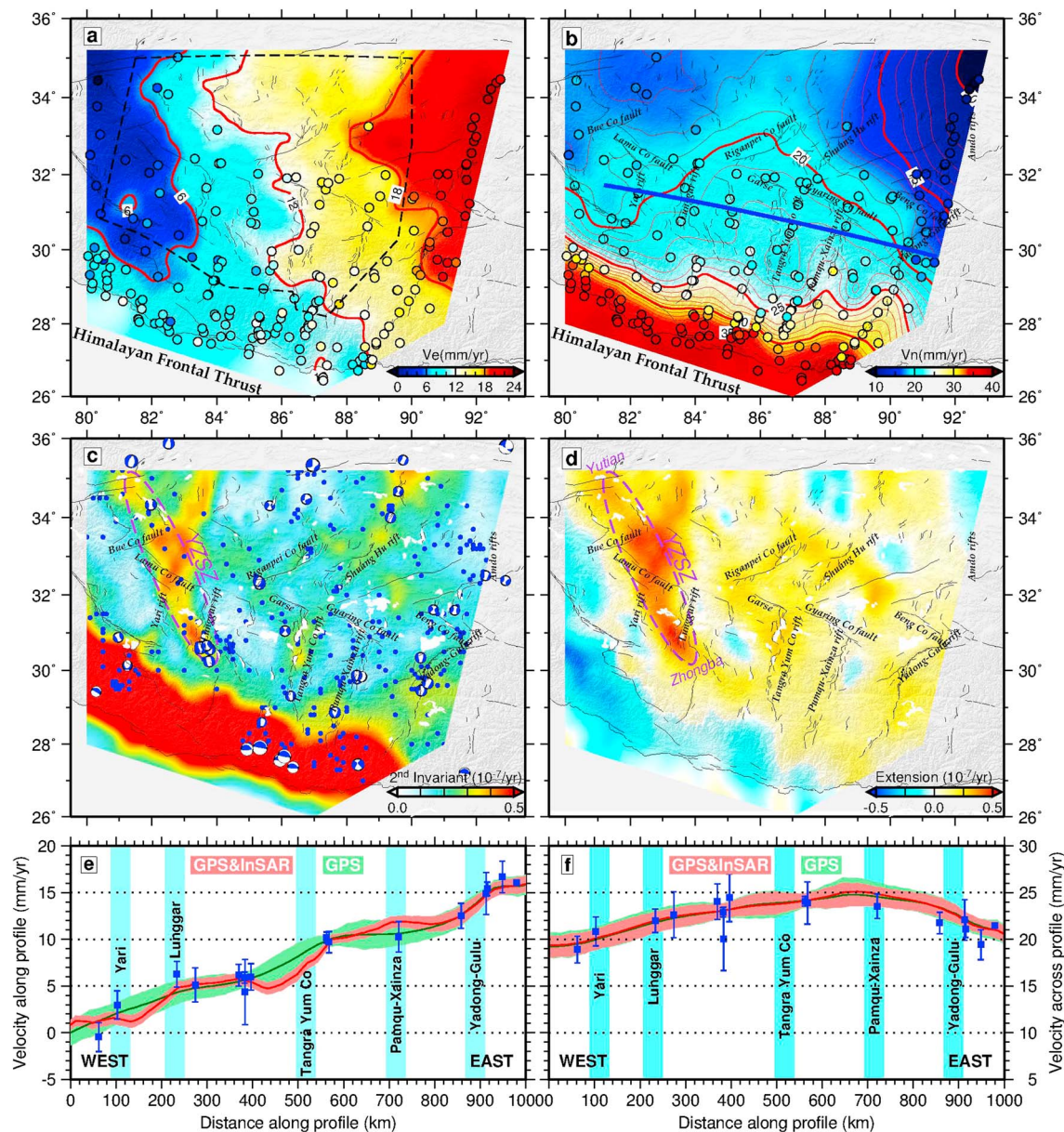


Figure 2. Velocity and strain rate fields in south-central Tibet derived from InSAR and GPS data. (a, b) East and north components of the velocity field. Color-coded circles indicate the corresponding GPS components used in the velocity field inversion. The dashed polygon delimits InSAR coverage. The red lines denote contours of the velocity field. The blue line indicates location of the velocity profile shown in Figures 2e and 2f. (c, d) Second invariants and extensional strain rate fields. The blue dots denote historical earthquakes. The ellipse highlights Yutian-Zhongba strain rate zone. (e, f) Red bands show velocities with 1σ errors along and across the profile. Green bands represent the corresponding components constrained by GPS alone. Blue squares denote the observed GPS velocities with 1σ errors. Cyan bars indicate locations of the major rift zones. GPS = Global Positioning System; InSAR = interferometric synthetic aperture radar.

In the Riganpei Co fault, paired with the Gyaring Co fault, we found similar left-lateral slip rate of about 2 ± 0.6 mm/year on the east and west segments. Again, these are lower than the rate of 6.6 mm/year with estimated locking depth of 14.5 km in Taylor and Peltzer (2006). For another set of conjugate faults, we found right-slip rate of $2-4 \pm 0.2$ mm/year in the Lamu Co fault (Figures 3f and 3g) and no apparent slip in the Bue Co fault (Figures 3h). This is consistent with the slip rate of 2.6 mm/year in the Lamu Co fault with estimated locking depth of 5.8 km found by Taylor and Peltzer (2006). While comparing slip rate, we should keep in mind its strong trade-off with locking depth. This resulted in large error intervals of the estimated locking depths in Taylor and Peltzer (2006), with average of ~ 30 km.

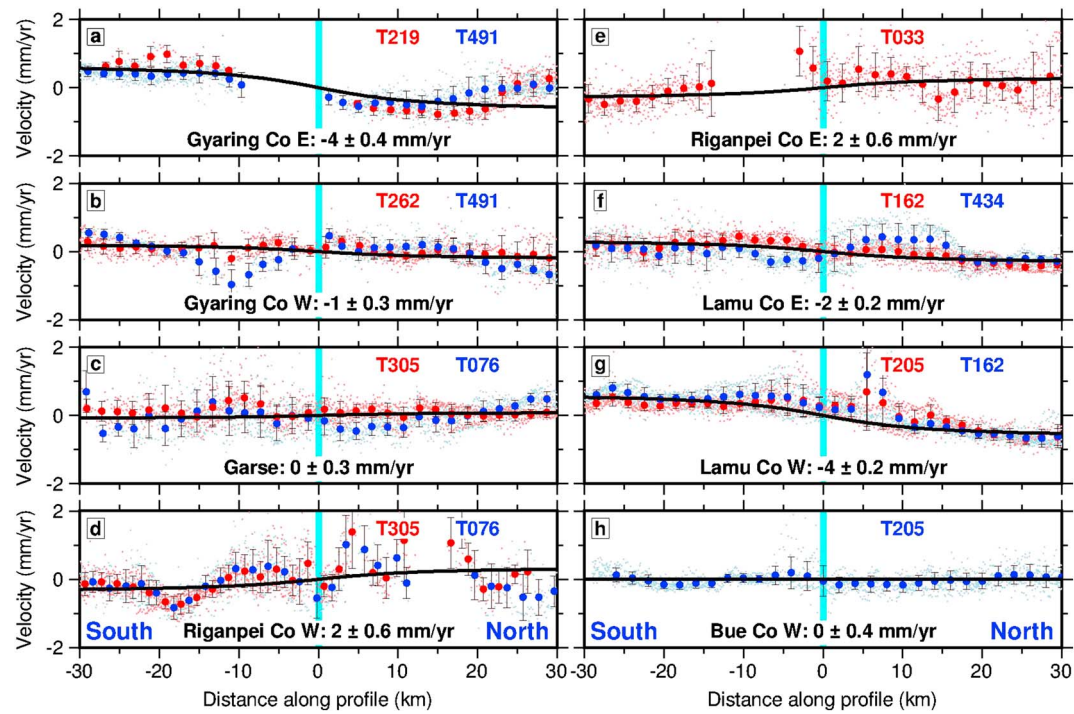


Figure 3. Slip rates of the conjugate strike-slip faults from eight profiles shown as thick blue lines in Figure 1b. Red and blue dots with 1σ error bars represent InSAR LOS velocities perpendicular to the profiles from two neighboring tracks as labeled. Cyan bars indicate locations of the faults. The black lines are LOS velocities predicted using an elastic dislocation model (Savage & Burford, 1973). Fault name and its slip rate are labeled at the bottom of each subplot, and positive represents left-lateral slip.

Our results agree with the sense of slip expected for the conjugate strike-slip fault systems, that is, left-lateral slip for NE striking faults and right-lateral slip for NW striking faults. But our estimate of slip rate is within 4 mm/year, consistent with available Holocene slip rate (Shi et al., 2014). The results agree with other conjugate strike-slip faults in further east of central Tibet, including Amdo-Sewa, Dongqiao, and Beng Co faults (Garthwaite et al., 2013), although the latter might be affected by long-term postseismic effects (Ryder et al., 2014).

4.2. Extension in Southern Tibet

In southern Tibet, north of the Himalayan arc, deformation is dominated by east-west extension via seven regularly spaced north-south trending rift systems (Armijo et al., 1986; Molnar & Lyon-Caen, 1989; Molnar & Tapponnier, 1978). Early studies suggested a total extension rate of 10 ± 6 mm/year from satellite imagery (Armijo et al., 1986) or 18 ± 9 mm/year from seismic moment release (Molnar & Lyon-Caen, 1989). Elliott et al. (2010) obtained an extension rate of 3–4 mm/year by summing 43 years of normal earthquakes, which is only $\sim 15\text{--}20\%$ of the total 21.6 ± 2.5 -mm/year extension across the plateau found using GPS (Zhang et al., 2004). Based on early GPS observations, Chen et al. (2004) estimated a total extension rate of 9.7 ± 3.0 mm/year for the rifts, of which about 1/2–2/3 was focused on the Yadong-Gulu Rift with most of the remainder in the Thakkola graben. Recent GPS data showed a total extension of ~ 15 mm/year across southern Tibet (Zheng et al., 2017), similar to the 13 ± 2 mm/year estimated by Chen et al. (2004), but the recent results appear to show strain to be fairly uniformly distributed on a length scale of $\sim 1,500$ km ($75^\circ\text{--}90^\circ\text{E}$; Zheng et al., 2017). However, the GPS sites are too sparsely distributed to reliably constrain spatial variations in the east-west extension rate.

We examined our velocity field across southern Tibet along a $N80^\circ\text{W}$ trending profile (Figure 2b). As expected, the total extension is ~ 15 mm/year, as that is constrained from GPS alone (blue squares in Figure 2e). However, the results reveal clear spatial variations along the profile. The strongest extension rates are across Lunggar, Tangra Yum Co, and Yadong-Gulu Rifts, each with approximately equal rates of $\sim 4\text{--}5$ mm/year. The extension rate of the Pamqu-Xainza Rift is only $\sim 1\text{--}2$ mm/year, and no clear extension is seen on the Yari Rift. Such features are also shown in the extensional strain rate field, which is derived by

projecting the strain rate tensors to N80°W (Figure 2d). The mean extensional strain rates are ~12 and ~14 nanostrain per year to the south and north of the BNS.

5. Discussion

5.1. Strain Rate Distribution

One important application of geodetic strain rates is to identify where strain is accumulating most rapidly and thus where earthquakes are most likely to occur (Bird et al., 2010). Our results in Figure 2c show a few zones with focused high strain rates. These are generally associated with major active structures and historical earthquakes. In the interior of the plateau, the most significant is the NNW-SSE elongated YZSZ. It aligns with the southern Lunggar Rift in the south, but we do not find clear active faults associated with the high strain rates for the rest of the zone. The strain rate field from GPS alone shows this feature as well, although with smaller magnitude (Figure S11), reinforcing the reliability of the signal. Several normal earthquakes have occurred along this zone, including the 2004–2008 Zhongba series of M_w 6.2–6.7 earthquakes and the 2008 M_w 7.1 Yutian earthquake. However, there is no earthquake with $M_w \geq 5.5$ in the past 30 years between Zhongba and Yutian; if strain accumulation and release are steady in time, this zone may be particularly at risk of future earthquakes.

The second invariant of strain rates are spatially variable along and between the rifts, showing relatively high strain rates aligned with the northern Tangra Yum Co Rift, the Shuang Hu Rift, and the southern Yadong-Gulu Rift. Unlike other rifts, strain rates are low in most of the Pumqu-Xainza Rift, where normal faulting earthquakes occurred in the 1990s (Wang et al., 2014).

The spatial variability of tectonic strain we observed in our recent geodetic data can be explained in three ways. First, it could represent a genuine spatial variability in the long-term strain rate, reflecting the underlying tectonic forcing and spatial variations in lithospheric rheology. Most models of the active deformation assume that present-day deformation represents the long-term average rate of deformation (e.g., England & Molnar, 2005; Kreemer et al., 2014; Thatcher, 2007). Alternatively, strain rates could vary in time, for example, due to earthquake cycle effects (e.g., Dolan & Meade, 2017; Graham et al., 2018). Hussain et al. (2018) showed that the strain rate on the North Anatolian Fault is constant for most of the earthquake cycle, except for the decade or so following a major earthquake. However, it is unclear whether this result holds for faults that are not major transform faults with tens of kilometers of cumulative offset. As geodetic data improve and time series lengthen, there are examples where geodetic strain rates have been observed to vary in time. For example, long-term accelerating slip was observed preceding the 2011 Tohoku-oki earthquake (Mavromatis, Segall & Johnson, 2014; Mavromatis, Segall, Uchida, et al., 2014) and on the creeping segment of the Central San Andreas Fault (Khoshmanesh & Shirzaei, 2018). In addition, there are a number of locations where the geodetic strain rate has shown to be inconsistent with the long-term tectonic strain rate, for example, Garlock Fault, California (Dolan et al., 2016; Peltzer et al., 2001). The third possibility could be the effect of listric fault geometry. Shallow fault dip to subhorizontal detachment at depth may partially explain the pattern of diffusive strain loading away from the surface traces of active normal faults, as suggested for the Basin and Range Province (Velasco et al., 2010). Further work on measuring long-term fault slip rates is required to make progress on resolving this important issue in southern Tibet.

5.2. Relationship Between Faulting and Strain

To test the importance of active faults on strain accumulation, we created spatial buffers around all the mapped active fault zones between the IYS and the JS and looked at the second invariant of strain rates inside these buffer zones (Figure S13a) compared to the strain rates outside (Figure S13b). We tested different buffer widths from 10 to 30 km on both sides of the faults. The average strain rate within the fault zones is ~20 nanostrain per year (orange bars in Figure S13c), which is only slightly larger than the average of ~18–19 nanostrain per year outside (blue bars in Figure S13c). To avoid effects of the high strain rates in the YZSZ, we also made statistics only for the eastern portion ($>84^\circ\text{E}$). This resulted in 18 versus 17 nanostrain per year within and outside the buffer zones.

We did similar statistics for the extensional strain rates in southern Tibet between the IYS and the BNS (Figures S13d–S13f). For a buffer width of 20 km, the average is 14 nanostrain per year within the rift zones, not much larger than the average of 10 nanostrain per year outside. For the eastern portion ($>84^\circ\text{E}$), the averages are 13 versus 11–12 nanostrain per year for buffer widths from 10 to 30 km. We therefore conclude that significant strain occurs outside the zones of active faulting.

5.3. Continental Deformation Models

How continents deform has been subject to much debate since the birth of plate tectonics. This debate has typically focused on whether continental deformation is largely block like (Tapponnier et al., 1982) or whether it can be described as a continuum (England & Houseman, 1986). These two kinds of models predict different characteristics about surface deformation: block-like models require high slip rates and focused strain on the major faults, while negligible deformation inside the blocks; continuum models predict relatively low slip rates on large faults and continuous strain distribution in the whole region. Geodetic velocity fields naturally act as an important tool to test different models. Until recently, sparse GPS measurements could be fit equally well using either block-like (Meade, 2007; Thatcher, 2007) or continuum models (England & Molnar, 2005). With the increasing number of GPS sites (Zheng et al., 2017), the velocity field presents diffuse deforming in western China and widespread dilatation at high elevations in Tibet, whereas deformation is negligible in several large regions and some major faults show strain concentrations. Neither of the models can adequately explain all these key features.

Considerable effort is being made to develop more complicated models to satisfy the GPS observations. In the block-like models, the number of blocks in central Asia required to match the geodetic observations has increased dramatically from 4 in Avouac and Tapponnier (1993) to 30 in Wang et al. (2017), and additional internal deformation has been introduced to account for large residuals within the blocks (Chen et al., 2004; Loveless & Meade, 2011). In the continuum models, spatial variations in viscosity have been also considered to produce focused strain accumulation on the major faults (Bendick & Flesch, 2013; Lechmann et al., 2011).

It is especially challenging for the existing models to fit the InSAR data, which are at much higher spatial resolution than GPS (Garthwaite et al., 2013; Wang & Wright, 2012). Like our previous study in western Tibet (Wang & Wright, 2012), here we have identified a few zones with focused high strain rates that appear like new block boundaries. Continuum models struggle to reproduce such features. However, the high strain zones do not always align with obvious tectonic features or join up in connected networks of blocks, as is required by block models. Considering all the key features from our InSAR/GPS velocity field, we suggest that the broad-scale velocity field is controlled by steady-state continuum mechanics, but earthquake cycle effects must be accounted for when examining the instantaneous present-day velocity field. In particular, repeated earthquakes on a fault zone will cause a long-term strain concentrations around the fault zone, if the relaxation time of the lower crust is longer than the interevent time (Hussain et al., 2018).

Acknowledgments

H. W. was supported by the NSFC grants (41672205, 41104016, and 41372221). Part of the work was conducted in the Abdus Salam International Centre for Theoretical Physics (ICTP) through a Regular Associateship awarded to H. W. T. J. W. was supported by the Natural Environment Research Council (NERC) through the Centre for the Observation and Modelling of Earthquakes, Volcanoes and Tectonics (COMET) and the LiCS large grant (NE/K010867/1). J. L.-Z. was supported by the NSFC grant (41761144065). ERS and Envisat data are copyrighted by ESA and were provided under the Dragon (5305) and category-1 (13757) projects. We thank Lucy Flesch, Manoochehr Shirzaei, and an anonymous reviewer for their constructive comments that helped improve the manuscript. We used the JPL/Caltech ROI_PAC software to process InSAR data, and the Generic Mapping Tools (Wessel and Smith, 1998) to prepare the figures. Our open-source software *II-RATE* is available at the website (<http://homepages.see.leeds.ac.uk/~earhw/software/pirate>).

6. Conclusions

We form velocity and strain rate fields in south-central Tibet by combining 208 GPS velocities from Zheng et al. (2017) with InSAR rate maps derived from 12 ERS/Envisat tracks. The good coverage of InSAR data significantly improves the accuracy and the spatial resolution of the present-day crustal deformation in south-central Tibet, which is remote and poorly investigated to date. The strain rate field shows that deformation is not evenly distributed across the region. A few active rifts, such as Lunggar, Tangra Yum Co, and Yudong-Gulu, have higher strain rates than the others. Some high strain rate zones are not associated with mapped faults, most notably the YZSZ. In central Tibet, the slip rates of all the conjugate strike-slip faults are within 4 mm/year. Such spatially variable distribution of strain rates reinforces the importance of geodetic data in seismic hazard assessment.

We find that current models are unable to explain the complex ongoing deformation in south-central Tibet: low slip rates on the conjugate strike-slip faults; similar strain rates inside and outside the mapped fault zones; focused high strain rates on a few fault zones. The increasing number of geodetic data requires a new generation of continental deformation model that likely requires time-dependent effects and lateral variations in strength.

References

- Armijo, R., Tapponnier, P., & Han, T.-L. (1989). Late Cenozoic right-lateral strike-slip faulting in southern Tibet. *Journal of Geophysical Research*, 94(B3), 2787–2838.
- Armijo, R., Tapponnier, P., Mercier, J. L., & Han, T.-L. (1986). Quaternary extension in southern Tibet: Field observations and tectonic implications. *Journal of Geophysical Research*, 91(B14), 13,803–13,872.
- Avouac, J.-P., & Tapponnier, P. (1993). Kinematic model of active deformation in central Asia. *Geophysical Research Letters*, 20(10), 895–898.

- Bendick, R., & Flesch, L. (2013). A review of heterogeneous materials and their implications for relationships between kinematics and dynamics in continents. *Tectonics*, 32, 980–992. <https://doi.org/10.1002/tect.20058>
- Biggs, J., Wright, T., Lu, Z., & Parsons, B. (2007). Multi-interferogram method for measuring interseismic deformation: Denali Fault, Alaska. *Geophysical Journal International*, 170(3), 1165–1179. <https://doi.org/10.1111/j.1365-246X.2007.03415.x>
- Bird, P., Kreemer, C., & Holt, W. E. (2010). A long-term forecast of shallow seismicity based on the Global Strain Rate Map. *Seismological Research Letters*, 82(2), 184–194.
- Chen, Q., Freymueller, J. T., Wang, Q., Yang, Z., & Xu, C. (2004). A deforming block model for the present-day tectonics of Tibet. *Journal of Geophysical Research*, 109(B01403). <https://doi.org/10.1029/2002JB002151>
- Desbrun, M., Meyer, M., Schroder, P., & Barr, A. H. (1999). Implicit fairing of irregular meshes using diffusion and curvature flow. *SIGGRAPH*, 99, 317–324.
- Doin, M.-P., Twardzik, C., Ducret, G., Lasserre, C., Guillason, S., & Jianbao, S. (2015). InSAR measurement of the deformation around Siling Co Lake: Inferences on the lower crust viscosity in central Tibet. *Journal of Geophysical Research: Solid Earth*, 120, 5290–5310. <https://doi.org/10.1002/2014JB011768>
- Dolan, J. F., McAuliffe, L. J., Rhodes, E. J., McGill, S. F., & Zinke, R. (2016). Extreme multi-millennial slip rate variations on the Garlock fault, California: Strain super-cycles, potentially time-variable fault strength, and implications for system-level earthquake occurrence. *Earth and Planetary Science Letters*, 446, 123–136.
- Dolan, J. F., & Meade, B. J. (2017). A comparison of geodetic and geologic rates prior to large strike-slip earthquakes: A diversity of earthquake-cycle behaviors? *Geochemistry, Geophysics, Geosystems*, 18, 4426–4436. <https://doi.org/10.1002/2017GC007014>
- Elliott, J. R., Biggs, J., Parsons, B., & Wright, T. J. (2008). InSAR slip rate determination on the Alyn Tagh Fault, northern Tibet, in the presence of topographically correlated atmospheric delays. *Geophysical Research Letters*, 35, L12309. <https://doi.org/10.1029/2008GL033659>
- Elliott, J. R., Walters, R. J., England, P. C., Jackson, J. A., Li, Z., & Parsons, B. (2010). Extension on the Tibetan Plateau: Recent normal faulting measured by InSAR and body wave seismology. *Geophysical Journal International*, 183(2), 503–535.
- Elliott, J. R., Walters, R. J., & Wright, T. J. (2016). The role of space-based observation in understanding and responding to active tectonics and earthquakes. *Nature Communications*, 7, 13844. <https://doi.org/10.1038/ncomms13844>
- England, P. C., & Houseman, G. A. (1986). Finite strain calculations of continental deformation: 2. Comparison with the India-Asia collision. *Journal of Geophysical Research*, 91, 3664–3676.
- England, P., & Jackson, J. (2011). Uncharted seismic risk. *Nature Geoscience*, 4, 348–349.
- England, P., & Molnar, P. (1997). Active deformation of Asia: From kinematics to dynamics. *Science*, 278(5338), 647–650.
- England, P., & Molnar, P. (2005). Late Quaternary to decadal velocity fields in Asia. *Journal of Geophysical Research*, 110, B12401. <https://doi.org/10.1029/2004JB003541>
- Farr, T. G., Rosen, P. A., Caro, E., Crippen, R., Duren, R., Hensley, S., et al. (2007). The Shuttle Radar Topography Mission. *Reviews of Geophysics*, 45, RG2004. <https://doi.org/10.1029/2005RG000183>
- Field, E., Arrowsmith, R., Biasi, G., Bird, P., Dawson, T., Felzer, K., et al. (2014). Uniform California Earthquake Rupture Forecast, version 3 (UCERF3) - the time-independent model. *Bulletin of the Seismological Society of America*, 104(3), 1122–1180. <https://doi.org/10.1785/0120130164>
- Garthwaite, M. C., Wang, H., & Wright, T. J. (2013). Broadscale interseismic deformation and fault slip rates in the central Tibetan Plateau observed using InSAR. *Journal of Geophysical Research: Solid Earth*, 118, 5071–5083. <https://doi.org/10.1002/jgrb.50348>
- Goldstein, R. M., & Werner, C. L. (1998). Radar interferogram filtering for geophysical applications. *Geophysical Research Letters*, 25(21), 4035–4038.
- Goldstein, R. M., Zebker, H. A., & Werner, C. L. (1988). Satellite radar interferometry: Two-dimensional phase unwrapping. *Radio Science*, 23(4), 713–720.
- Grafarend, E. W. (1985). Variance-covariance component estimation: Theoretical results and geodetic applications. *Statistics and Decision, Supplement*, 2, 407–441.
- Graham, S. E., Loveless, J. P., & Meade, B. J. (2018). Global plate motions and earthquake cycle effects. *Geochemistry, Geophysics, Geosystems*, 19, 2032–2048. <https://doi.org/10.1029/2017GC007391>
- Hussain, E., Wright, T. J., Walters, R. J., Bekaert, D. P. S., Lloyd, R., & Hooper, A. (2018). Constant strain accumulation rate between major earthquakes on the North Anatolian Fault. *Nature Communications*, 9(1392). <https://doi.org/10.1038/s41467-018-03739-2>
- Ingleby, T., & Wright, T. J. (2017). Omori-like decay of postseismic velocities following continental earthquakes. *Geophysical Research Letters*, 44, 3119–3130. <https://doi.org/10.1029/2017GL072865>
- Jackson, J. (2001). Living with earthquakes: Know your faults. *Journal of Earthquake Engineering*, 5, 5–123.
- Khoshmanesh, M., & Shirzaei, M. (2018). Multiscale dynamics of aseismic slip on Central San Andreas fault. *Geophysical Research Letters*, 45, 2274–2282. <https://doi.org/10.1002/2018GL077017>
- Kreemer, C., Blewitt, G., & Klein, E. C. (2014). A geodetic plate motion and Global Strain Rate Model. *Geochemistry, Geophysics, Geosystems*, 15, 3849–3889. <https://doi.org/10.1002/2014GC005407>
- Lechmann, S. M., May, D. A., Kaus, B. J. P., & Schmalholz, S. M. (2011). Comparing thin-sheet models with 3-D multilayer models for continental collision. *Geophysical Journal International*, 187(1), 10–33.
- Liang, S., Gan, W., Shen, C., Xiao, G., Liu, J., Chen, W., et al. (2013). Three-dimensional velocity field of present-day crustal motion of the Tibetan Plateau derived from GPS measurements. *Journal of Geophysical Research: Solid Earth*, 118, 5722–5732. <https://doi.org/10.1002/2013JB010503>
- Liu, Z., & Bird, P. (2008). Kinematic modelling of neotectonics in the Persia-Tibet-Burma orogen. *Geophysical Journal International*, 172(2), 779–797.
- Loveless, J., & Meade, B. (2011). Partitioning of localized and diffuse deformation in the Tibetan Plateau from joint inversions of geologic and geodetic observations. *Earth and Planetary Science Letters*, 303, 11–24.
- Mavrommatis, A. P., Segall, P., & Johnson, K. M. (2014). A decadal-scale deformation transient prior to the 2011 Mw 9.0 Tohoku-oki earthquake. *Geophysical Research Letters*, 41, 4486–4494. <https://doi.org/10.1002/2014GL060139>
- Mavrommatis, A. P., Segall, P., Uchida, N., & Johnson, K. M. (2014). Long-term acceleration of aseismic slip preceding the Mw 9 Tohoku-oki earthquake: Constraints from repeating earthquakes. *Geophysical Research Letters*, 42, 9717–9725. <https://doi.org/10.1002/2015GL066069>
- Meade, B. J. (2007). Present-day kinematics at the India-Asia collision zone. *Geology*, 35(1), 81–84.
- Molnar, P., & Lyon-Caen, H. (1989). Fault plane solutions of earthquakes and active tectonics of the Tibetan Plateau and its margins. *Geophysical Journal International*, 99(1), 123–154.
- Molnar, P., & Tapponnier, P. (1975). Cenozoic tectonics of Asia: Effects of a continental collision. *Science*, 189(4201), 419–426.

- Molnar, P., & Tapponnier, P. (1978). Active tectonics of Tibet. *Journal of Geophysical Research*, 83(B11), 5361–5375.
- Pagli, C., Wang, H., Wright, T. J., Calais, E., & Lewi, E. (2014). Current plate boundary deformation of the Afar rift from a 3-D velocity field inversion of InSAR and GPS. *Journal of Geophysical Research: Solid Earth*, 119, 8562–8575. <https://doi.org/10.1002/2014JB011391>
- Parsons, B., Wright, T., Rowe, P., Andrews, J., Jackson, J., Walker, R., et al. (2006). The 1994 Sefidabeh (eastern Iran) earthquake revisited: New evidence from satellite radar interferometry and carbonate dating about the growth of an active fold above a blind thrust fault. *Geophysical Journal International*, 164, 202–217.
- Peltzer, G., Crampé, F., Hensley, S., & Rosen, P. (2001). Transient strain accumulation and fault interaction in the Eastern California shear zone. *Geology*, 29(11), 975–978.
- Rosen, P. A., Hensley, S., Peltzer, G., & Simons, M. (2004). Updated repeat orbit interferometry package released. *EOS Transactions*, 85(5), 47.
- Ryder, I., Wang, H., Bie, L., & Rietbrock, A. (2014). Geodetic imaging of late postseismic lower crustal flow in Tibet. *Earth and Planetary Science Letters*, 404, 136–143.
- Savage, J. C., & Burford, R. O. (1973). Geodetic determination of relative plate motion in central California. *Journal of Geophysical Research*, 78, 832–845.
- Savage, J. C., Gan, W., & Svarc, J. L. (2001). Strain accumulation and rotation in the Eastern California Shear Zone. *Journal of Geophysical Research*, 106(10), 21,995–22,007.
- Shi, X., Kirby, E., Lu, H., Robinson, R., Furlong, K. P., & Wang, E. (2014). Holocene slip rate along the Gyaring Co Fault, central Tibet. *Geophysical Research Letters*, 41, 5829–5837. <https://doi.org/10.1002/2014GL060782>
- Styron, R. H., Taylor, M. H., & Murphy, M. A. (2011). Oblique convergence, arc-parallel extension, and the role of strike-slip faulting in the High Himalaya. *Geosphere*, 7, 582–596.
- Tapponnier, P., Peltzer, G., Le Dain, A. Y., Armijo, R., & Cobbold, P. (1982). Propagating extrusion tectonics in Asia: New insights from simple experiments with plasticine. *Geology*, 10, 611–617.
- Taylor, M., & Peltzer, G. (2006). Current slip rates on conjugate strike-slip faults in central Tibet using synthetic aperture radar interferometry. *Journal of Geophysical Research*, 111, B12402. <https://doi.org/10.1029/2005JB004014>
- Taylor, M., & Yin, A. (2009). Active structures of the Himalayan-Tibetan orogen and their relationships to earthquake distribution, contemporary strain field, and Cenozoic volcanism. *Geosphere*, 5(3), 199–214.
- Taylor, M., Yin, A., Ryerson, F. J., Kapp, P., & Ding, L. (2003). Conjugate strike-slip faulting along the Bangong-Nujiang suture zone accommodates coeval east-west extension and north-south shortening in the interior of the Tibetan Plateau. *Tectonics*, 22(4), 1044. <https://doi.org/10.1029/2002TC001361>
- Thatcher, W. (2007). Microplate model for the present-day deformation of Tibet. *Journal of Geophysical Research*, 112, B01401. <https://doi.org/10.1029/2005JB004244>
- Velasco, M. S., Bennett, R. A., Johnson, R. A., & Hreinsdóttir, S. (2010). Subsurface fault geometries and crustal extension in the eastern Basin and Range Province, western U.S. *Tectonophysics*, 488(1), 131–142.
- Walters, R. J., Parsons, B., & Wright, T. J. (2014). Constraining crustal velocity fields with InSAR for Eastern Turkey: Limits to the block-like behavior of Eastern Anatolia. *Journal of Geophysical Research: Solid Earth*, 119, 5215–5234. <https://doi.org/10.1002/2013JB010909>
- Wang, H., Elliott, J. R., Craig, T. J., Wright, T. J., Liu-Zeng, J., & Hooper, A. (2014). Normal faulting sequence in the Pumqu-Xainza Rift constrained by InSAR and teleseismic body-wave seismology. *Geochemistry, Geophysics, Geosystems*, 15, 2947–2963. <https://doi.org/10.1002/2014GC005369>
- Wang, W., Qiao, X., Yang, S., & Wang, D. (2017). Present-day velocity field and block kinematics of Tibetan Plateau from GPS measurements. *Geophysical Journal International*, 208, 1088–1102. <https://doi.org/10.1093/gji/ggw445>
- Wang, H., & Wright, T. J. (2012). Satellite geodetic imaging reveals internal deformation of western Tibet. *Geophysical Research Letters*, 39, L07303. <https://doi.org/10.1029/2012GL051222>
- Wang, H., Wright, T. J., & Biggs, J. (2009). Interseismic slip rate of the northwestern Xianshuhei fault from InSAR data. *Geophysical Research Letters*, 36, L03302. <https://doi.org/10.1029/2008GL036560>
- Wang, H., Wright, T. J., Yu, Y., Lin, H., Jiang, L., Li, C., & Qiu, G. (2012). InSAR reveals coastal subsidence in the Pearl River Delta, China. *Geophysical Journal International*, 191(3), 1119–1128. <https://doi.org/10.1111/j.1365-246X.2012.05687.x>
- Wright, T. J., Elliott, J. R., Wang, H., & Ryder, I. (2013). Earthquake cycle deformation and the Moho: Implications for the rheology of continental lithosphere. *Tectonophysics*, 609, 504–523.
- Zhang, P.-Z., Shen, Z., Wang, M., Gan, W., Bürgmann, R., Molnar, P., et al. (2004). Continuous deformation of the Tibet Plateau from global positioning system data. *Geology*, 32(9), 809–812.
- Zheng, G., Lou, Y., Wang, H., Geng, J., & Shi, C. (2018). Shallow seismicity forecast for the India-Eurasia collision zone based on geodetic strain rates. *Geophysical Research Letters*, 45, 8905–8912. <https://doi.org/10.1029/2018GL078814>
- Zheng, G., Wang, H., Wright, T. J., Lou, Y., Zhang, R., Zhang, W., et al. (2017). Crustal deformation in the India-Eurasia collision zone from 25-years of GPS measurements. *Journal of Geophysical Research: Solid Earth*, 122, 9290–9312. <https://doi.org/10.1002/2017JB014465>